Feasibility of Integrating Bimetallic Au-Ag Non-Alloys Nanoparticles Embedded in Reduced Graphene Oxide Photodetector

Nurul Syazwani ROHIZAT[1], Muhammad Nur Syafiq MOHAMAD ISMAIL[1], Muhammad Aiman Saufi AHMAD FAHRI[1,2], Chee Leong TAN[3], and Rozalina ZAKARIA[1*]

[1]*Photonics Research Center, Faculty of Science, University of Malaya, Kuala Lumpur 50603, Malaysia*

[2]*Department of Physics, Faculty of Science, University of Malaya, Kuala Lumpur 50603, Malaysia*

[3]*School of Electronic and Optical Engineering and College of Microelectronics, Nanjing University of Posts and Telecommunications, Nanjing 210023, China*

[*]Corresponding author: Rozalina ZAKARIA E-mail: rozalina@um.edu.my

Abstract: To coordinate the resonant wavelength of the plasmonic nanoparticles (NPs), the emission band of the reduced graphene oxide (rGO) photodetector at the NIR-region is crucial for the optimal plasmon-enhanced luminescence in the device. In contrast to monometallic NPs, where limits the dimensions and extended resonant wavelength, we integrated an Au-Ag bimetallic NPs (BMNPs) to enable resonance tuning at the longer wavelength at the excitation source of 785 nm. These features showed an increase in radiative recombination rates as well as the quantum yield efficiency of the device. The BMNPs were produced from the dewetting process of 600 ℃ and 500 ℃, both at 1 min after the deposition thickness layer of Au (8 nm) and Ag (10 nm) on the Si substrate using the electron-beam evaporation process. Our BMNPs-rGO photodetector exhibited the responsivity of 2.25 $A \cdot W^{-1}$, Jones of specific detectivity of 2.45×10^{11} Jones, and external quantum efficiency (EQE) of 356%. The rise time and fall time for the photodetector were 32 ns and 186 ns, respectively. This work provided an essential information to enable the versatile plasmon-enhanced application in 2-dimensional (2D) material optoelectronic devices.

Keywords: Au-Ag bimetallic nanoparticles; rGO; photodetector

Citation: Nurul Syazwani ROHIZAT, Muhammad Nur Syafiq MOHAMAD ISMAIL, Muhammad Aiman Saufi AHMAD FAHRI, Chee Leong TAN, and Rozalina ZAKARIA, "Feasibility of Integrating Bimetallic Au-Ag Non-Alloys Nanoparticles Embedded in Reduced Graphene Oxide Photodetector," *Photonic Sensors*, 2023, 13(3): 230307.

1. Introduction

Plasmonic metal nanoparticles attracts a great interest in a broad range of applications in the field of opto-electronics and sensing applications. Noble metal nanoparticles namely Au [1], Ag [2], Cu [3], and Pt [4] show the strong optical resonance under the excitation of electromagnetic radiation due to the localized surface plasmon resonance (LSPR). Immense electromagnetic fields and intense plasmon absorption bands are generated due to the strong light-scattering from metal nanoparticles due to the excitation of LSPR [5, 6]. In many photovoltaic applications, the LSPR effects have been observed

Received: 23 August 2022 / Revised: 24 October 2022

DOI: 10.1007/s13320-023-0679-8
Article type: Regular

using metallic nanoparticles in broad applications, like Ag nanostructures in organic solar cells [7, 8] which enables to trap the incident light, thus reducing the reflection and increasing the efficiency of the device. The LSPR induced by Au nanoparticles also plays a vital role by improving the performance with the combination of 2-dimensional (2D) materials such as the p-MoS_2/n-ZnO heterostructure photodetector [9]. Furthermore, ZnO nanorods display an enhancement in the ultra-violet (UV) photodetection with the addition mono of Cu/Al nanoparticles by strengthening the LSPR coupling with the ZnO nanorods [10]. As one of the LSPR factors are the shape and size of the particles, the metallic nanoparticle can be fabricated by one of the least complicated as thermal annealing where it involves the modification of the surface morphology of the metallic layer according to temperature and time. The thin metallic layer deposited through the electron beam evaporation machine is in the metastable condition and upon receiving a thermal impetus, the atoms at the surface migrate to form individual's islands which ultimately produce metallic nanoparticles [11]. In the past years, there are many research projects, which have produced metallic nanoparticles with distinct morphology and orientations to design and fabricate highly responsive and efficient plasmonic photodetectors [12, 13].

Photodetectors principally emerge as an electronic device which can convert electromagnetic wave signals. Photodetectors in the visible light region are extensively used in many areas including remote sensing, thermal imaging, environmental monitoring, and telecommunications [14]. Photodetectors based on 2D materials have opened prospects due to their natural atom-thickness, distinctive quantum confinement, and electronic as well as photoelectric properties [15–17]. 2D materials, namely graphene, black phosphorus, and other transition metal dichalcogenides, have key properties that influence the semiconductor's electrical and optical properties from their bandgap. Specifically, these 2D materials are exemplified to exhibit a highly tunable bandgaps [18], accomplish by controlling several layers [19], heterostructure [20, 21], and converting as an external electric field.

Graphene is a 2D single layer material originating from bulk graphite. It consists of sp^2 hybridization bonded carbon atoms arranged in a hexagonal honeycomb crystal lattice [22]. Graphene oxide (GO) is typically produced from bulk graphite using modified Hummer's method, which consists of one or a few atomic layered materials from oxidation of graphite. Various reductants have been studied in recent years to transform GO to rGO. The latter contributes from the size and layers of flakes and the type and proportion of defects in graphene layers [22]. Thus far, insignificant-dark current and high-responsivity photodetectors are essential for the growth of the technology. Therefore, if these challenges can be resolved, many exceptional realizations are anticipated to be achieved by the 2D material photodetectors. This includes the ultra-high responsivity (10^5 $A \cdot W^{-1}$) [23], ultra-fast light response (1.1 ps) [24, 25], broad detection band (375 nm to 118.8 μm) [26], and ultra-sensitive photodetection ($1 V \cdot \mu W^{-1}$) [27].

To further distinguish the coupling effect between adjacent nanoparticles and the tunability of the resonance wavelength, the finite-difference time-domain (FDTD) is applied to simulate the light scattering from these metal particles [28]. Specifically, Au-Ag bimetallic non-alloyed NPs (BMNPs), which combine the superiorities of Ag NPs in the plasmonic sensitivity and chemical stability of Au NPs, have been displayed to enhance the light absorption across a broad range of wavelengths effectively. It can thus be suggested that BMNPs are supreme for applications of the solar cell compared with single-type metallic NPs, inducing the light-stimulated resonance advantage at only particular wavelength within a small

wavelength range [20, 29]. Therefore, in this work, we investigated the enhancement of photoresponse at NIR-region photodetectors integration of plasmonic BMNPs on rGO in comparison with bare rGO.

2. Experimental details

The Au-Ag nanoparticles were synthesized through two main processes: the first was thin films deposition and followed by thermal annealing. The thin films were prepared on the silicon substrate using the electron-beam (e-beam) evaporation for morphological and structural characterization, and for the fabrication of the photodetector device. Initially, the substrates were submitted to the three-step cleaning process before the deposition to remove any impurities. All steps were done for 5 min each under sonication. The three-steps were firstly cleaning the substrates in acetone, then followed by rinsing in isopropanol and finished off with subsequent rinsing with distilled water. Lastly, the substrates were dried using nitrogen gas after the final cleaning step.

Next, the deposition process would take place using an e-beam system. The pressure of the deposition chamber was voided to be below 1×10^{-6} Torr using the vacuum pump. The deposition rate was kept low at about $0.2\,A\cdot s^{-1}$ – $0.5\,A\cdot s^{-1}$ to revamp the uniformity of the thin films over a large surface area. These deposition conditions were maintained for both Au and Ag metals. After the first deposition, the as-deposited 8 nm Au thin film was subjected to thermal annealing to foster the growth of Au nanoparticles. It was expected to form hemisphere-shaped particles and nano islands. A 10 nm Ag thin film was deposited subsequently to the Au NPs and undergone the thermal annealing after that. The first thermal annealing was set at a temperature T_1 = 600 ℃ (Au NPs) and the second thermal annealing was set at a temperature T_2 = 500 ℃ (Ag NPs). Each annealing process was conducted for 1 min and was cooled down to room temperature. T_1 was intent to incite the agglomeration of Au NPs to impede the formation of the metal NPs alloy. This was an essential stage for the formation of non-alloy bimetallic nanoparticles, as reported in the previous work by the authors as reported in [30]. Furthermore, If $T_2 < T_1$, the Au NPs were prohibited to be intricated with the Ag thin films. Mainly, the bimetallic structures of Au-Ag NPs were formed by first depositing the Au metals, and then followed by thermal annealing at T_1 to form the Au NPs. Then, the subsequent deposit of the Ag thin film on the Au NPs would undergo the second thermal annealing at T_2. In this study, two kinds of metals, Au and Ag, were selected due to their significant difference at the LSPR wavelength. It was around 600 nm for Au and 400 nm for Ag. Besides, it was also due to the considerable gap between the melting temperatures of Au and Ag metals [31].

The morphology of the nanostructures images was analyzed by utilizing the field emission gun-based scanning electron microscope (FE-SEM) and using a model of FEI Quanta 400F. The study of the nanoparticles size was carried out using ImageJ, an image analysis software (https:imagej.nih.gov/ij/). The absorbance spectrum of the metallic nanoparticles has been measured using the ultraviolet (UV) spectrometer (PerkinElmer, USA).

The next step after the synthesis of nanoparticles was to deposit the electrode. The Cr/Au electrode was deposited using the e-beam evaporation method as previously discussed. The layer of the Cr/Au layer was deposited to 5 nm and 80 nm, respectively. The Cr layer was employed to improve the adhesion of the Au layer.

Graphene oxide (GO) was purchased from Graphenea with a concentration of 4 mg/ml. The GO solution was diluted with ethanol which acted as a solvent. The newly diluted solution was mixed to a ratio 1:15 (GO:ethanol). This approach was to

enhance the dispersion of GO [32]. Then, the new GO solution was sonicated for 2 h to ensure that the solution was stable and uniform. After that, the deposition of GO was executed by the spray deposition technique. For each deposition, a volume of 10 ml of the GO solution was applied. The substrate was placed on a heated 180 ℃ hotplate for 3 min and at the same time the GO deposition process was conducted. The purpose was to expedite the evaporation of the solvent and for the reduction of GO to rGO to occur. The effective contact area of the fabricated devices was 1×1.5 cm^2. Figure 1(a) presents the deposition as the bare GO. Figure 1(b) illustrates the sequence of the fabrication process from the deposition of Au, thermal annealing, followed by Ag deposition, the formation of NPs after thermal annealing and contact deposition for the photodetector.

The current-voltage (*I-V*) characterization was performed using Keithley 2410, a 1000 V, 1 A, 20 W source meter unit (Tektronix Instruments, USA). The measurements of photoresponse (*I-t*) were measured using DLM 2054 500 MHz mixed signal oscilloscope (Yokogawa, Japan) and DS345 30 MHz synthesized function generator (Stanford Research Systems, USA). The light-emitting diode (LED) of the NIR 785 nm wavelength was applied to excite the photodetectors. The NIR-LED power intensity was calibrated and measured using an optical power meter (Thorlabs, USA). All the measurements of the photocurrent were taken under the dark and illumination condition. The dark box was utilized when dark current measurements were carried out to remove the interference of ambient light.

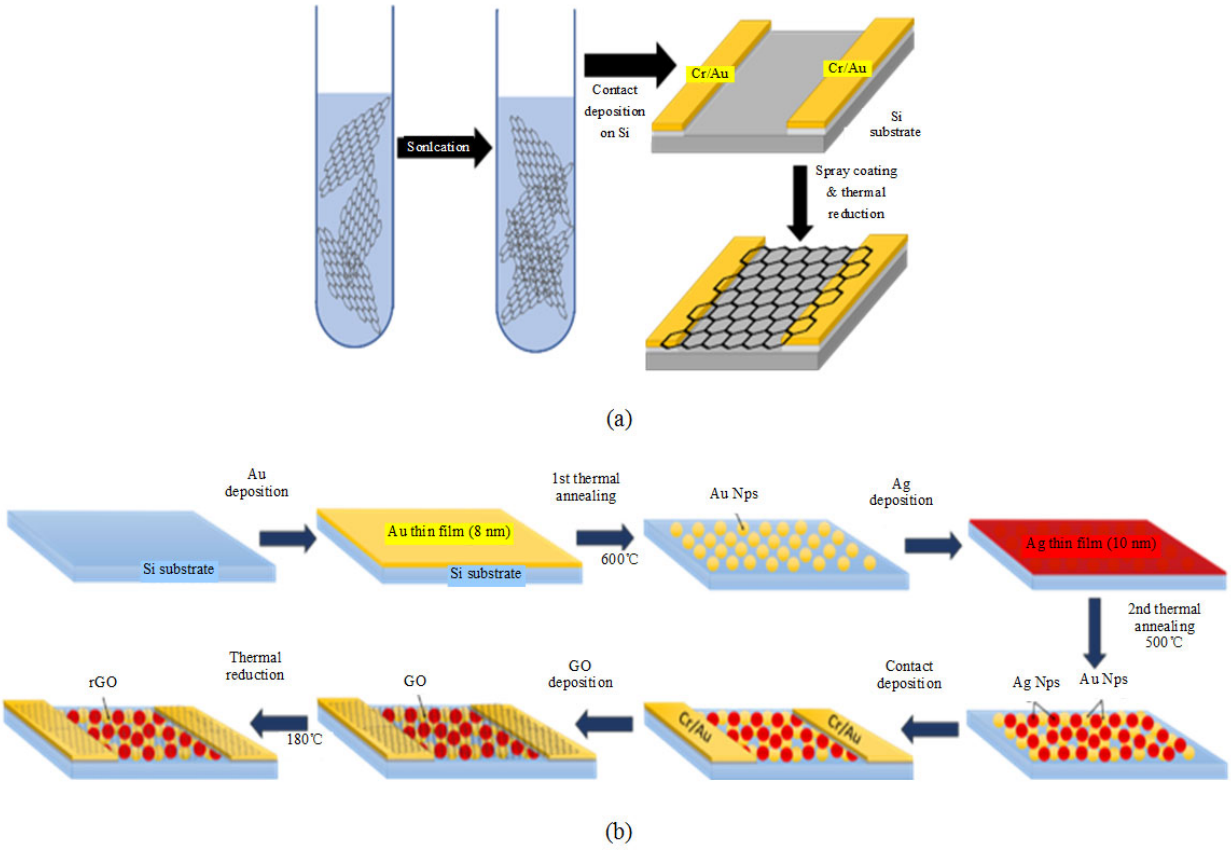

Fig. 1 Steps of fabrication process from (a) GO solution deposited on the substrate via spray deposition technique and (b) process of deposition thin layer, to formation of the NPs and photodetector.

3. Results and discussion

3.1 Optical characterization of monometallic Au, Ag, and bimetallic Au-Ag

Figure 2 displays the FESEM images of mono- and BMNPs. Initially, a thin Au metal film was deposited on the substrate and annealed at 600 ℃ for 1 min producing the monometallic structure of Au as shows in Fig. 2(a). The Ag thin film undergone a similar process and was annealed at 500 ℃ for 1 min with NPs formation as shown in Fig. 2(b). In Fig. 2(c), it is fascinatingly observed that the bimetallic non-alloyed Au-Ag NPs exhibited the ability to distribute evenly on the substrate. The FESEM image displayed that the two-step evaporation procedure successfully formed isolated of non-alloyed NPs. Besides, Au and Ag NPs proved that they could be clustered, monodispersed, and not aggregated. The size distribution of the nanoparticles was calculated and represented in the corresponding histogram as in inset images in all figures. The displayed FESEM image was taken at magnification of 100000x. It could be observed from the histogram (inset images) in Fig. 3 where all nanoparticles sizes were ranging from 45 nm to 100 nm. The annealing temperature of Ag, T_2, which was lower than the annealing temperature of Au, T_1($T_2 < T_1$), yielded that the Ag and AuNPs were sintered but separated compositionally [25].

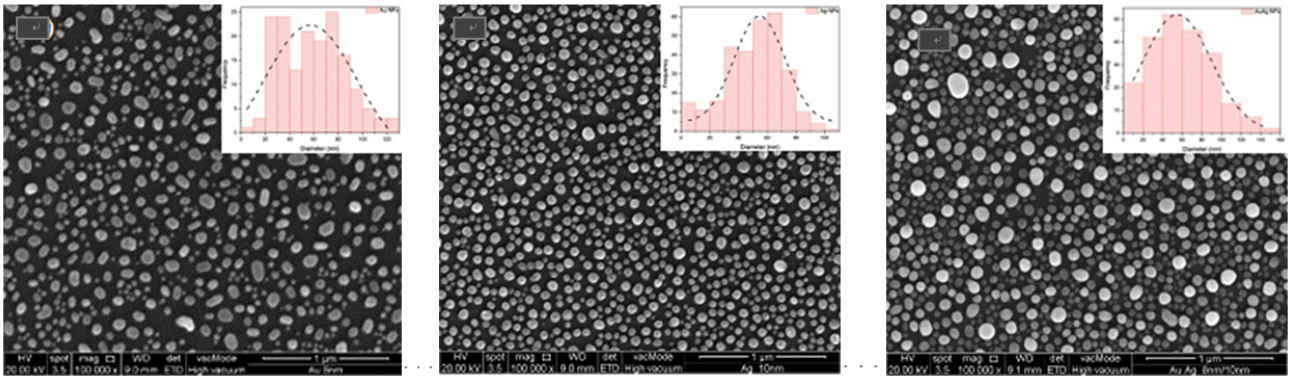

(a) (b) (c)

Fig. 2 FE-SEM images of (a) Au NPs, (b) Ag NPs, and (c) Au-Ag NPs. Inset images show the histogram distribution for each structure with the corresponding size of NPs.

3.2 Finite difference time domain (FDTD) for mono- and bimetallic structure

In this work, the FDTD method (Lumerical) was used to set up the mono- and BMNPs for simulation based on experimental findings. The FDTD was based on the Yee algorithm that used the leapfrog arrangement in order to satisfy the second order accuracy [28]. On the other hand, due to its versatility, the FDTD method of electrodynamic calculation was chosen to observe the results for the continuous wideband and multi-wavelength electromagnetic excitation simultaneously. The data of the complex relative dielectric constant of each material were obtained from the material database, CRC, while the complex refractive index of rGO was taken from Stefan *et al*. [33]. The boundary conditions were set to the perfect matched layer (PML) in the Z direction to truncate the travelling evanescent waves and be periodic in the X and Y directions. The incident electromagnetic waves were set to be in the 300 nm – 1100 nm wavelength range from the visible to near-infrared region. The monitor box was set up to analyze the electric field and permittivity, thus observing the absorption spectra of the metallic nanoparticles. The result from Au-Ag BMNPs simulation was then further continued to include a multilayer rGO with a thickness of 5 nm on the top of the NPs.

Figures 3(a) – 3(d) show the diagrams of the simulation setups with Au and Ag sizes of 90 nm and 54 nm respectively following from the selected areas in the FE-SEM experimental result images shown in the inset of the diagrams. The simulation structures are shown in Fig. 3(a) for the monometallic Au and Fig. 3(b) for the monometallic Ag, and Fig. 3(c) shows the bimetallic Au-Ag structures with the optimum size and dimension. Figure 3(d) depicts the side view of the composite structure of Au-Ag BMNPs with the rGO layer. The optical absorption results are shown in Figs. 3(e) – 3(h) for the monometallic Au with the LSPR peak at 570 nm, Ag with its peak at 474 nm, Au-Ag BMNPs' peak at 783 nm, and the composite structure with rGO with the highest peak at 825 nm.

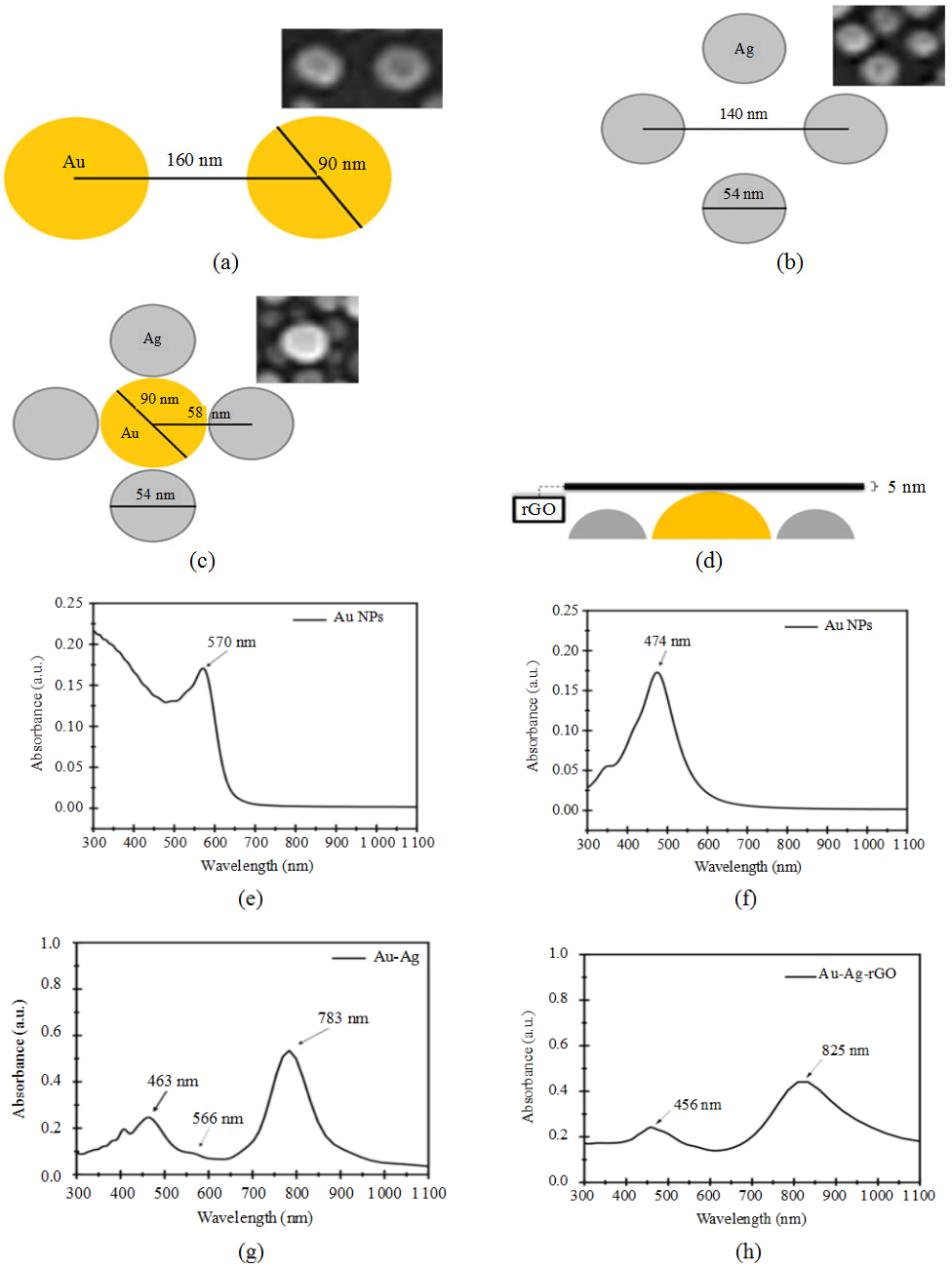

Fig. 3 FDTD simulation diagram for (a) monometallic Au, (b) monometallic Ag, (c) Au-Ag bimetallic, (d) Au-Ag bimetallic with rGO, and (e) – (h) normalized absorbances from 300 nm to 1 100 nm of the VIS-NIR excitation wavelength for Au, Ag, Au-Ag BMNPs, Au-Ag, and rGO composite structure.

The first two results of Au NP and Ag NP showed consistent LSPR peaks when compared with the typical peaks for those nanoparticles [29, 34]. The absorption spectrum for BMNPs showed a higher intensity at 780 nm, where it was likely due to the LSPR effect from the combination of Au and Ag NPs [35]. Then by using the same structure as the Au-Ag BMNPs but with an addition of the rGO layer above the nanoparticles, it could be seen that the 780 nm peak became red-shifted to 800 nm above while also being broader to the longer wavelength. This broadening phenomenon could likely be attributed to the interaction between plasmons located between the Au and Ag BMNPs and plasmons located between rGO and BNMPs. Thus, it could be inferred that BMNPs of Au and Ag could be tuned and prominently enhance the absorption of rGO in the NIR region.

3.3 Electrical characterization of bimetallic Au-Ag NPs-rGO PD

Non-alloyed BMNPs incorporating rGO PD and bare rGO PD were studied and compared with rGO PD function as a reference. The *I-V* characteristic was conducted in the dark condition and under the irradiation. In this study, the power intensity of the 785 nm NIR-LED was varied from 0.03 $mW \cdot cm^{-2}$ to 15.08 $mW \cdot cm^{-2}$. Figures 4 (a) – 4(b) illustrate the photocurrent responses with the voltage range of ± 30 V in both conditions with 100% light intensity of the 785 nm light source. It is observed that the dark current and photocurrent of the bimetallic Au-Ag NPs device display a big difference. The net photocurrent I_{ph} can be calculated with the total current subtracting the dark current as expressed in (1):

$$I_{ph} = I_{light} - I_{dark} \quad (1)$$

where I_{light} is the current under the NIR-LED irradiation, and I_{dark} is the dark current. When the Au-Ag NPs PD was illuminated, the current at 10 V increased from 3.15×10^{-5} A (dark condition) to 1.50×10^{-3} A under the NIR light. Instigated by the interface of the non-alloyed bimetallic Au-Ag NPs and rGO photoconductive response, a rise in the current on/off ratio (I_{light}/I_{dark}) of 10^2 was induced. This current on/off ratio was due to the integration of the non-alloyed bimetallic NPs to the device. Contrasting with the bare rGO PD, a significant difference of the increased current was recorded which only showed a small increase from 2.06×10^{-4} A (dark condition) to 9.61×10^{-4} A (illuminated).

In addition, this behavior indicated that the Schottky type barrier formation happened when the rGO layer absorbed the incident light [36]. The excitons (electron-hole pairs) were acquired at the Schottky-like metal-rGO interface and also these excitons could be dissociated into free carriers with the aid from defects in rGO with several of them having adequate energy to overcome the Schottky barrier [36]. Surface plasmons improved the photocurrent of this device via two approaches: the generated hot electrons from plasmon decay were transferred in the metal where the near-field and direct excitons were escalated for an increase in the responsivity [37].

Interestingly, the dark current of the BMNPs device was observed to be smaller than the dark current of rGO as shown in Fig. 4(c) and at power of 15.08 $mW \cdot cm^{-2}$ as in Fig. 4(d). Theoretically, it is better for the device to have the low dark current for the better performance [38]. On the other hand, despite having the lower dark current than the bare rGO, under the illumination of 785 nm light, Au-Ag exhibited the lower current than the bare rGO in the range of –30 V to –25 V. However, between –25 V and 30 V, the current of Au-Ag was greater than that of the bare rGO. It could clearly be seen that the photocurrents of the BMNPs-rGO PD and bare rGO were rising in tune with the voltage.

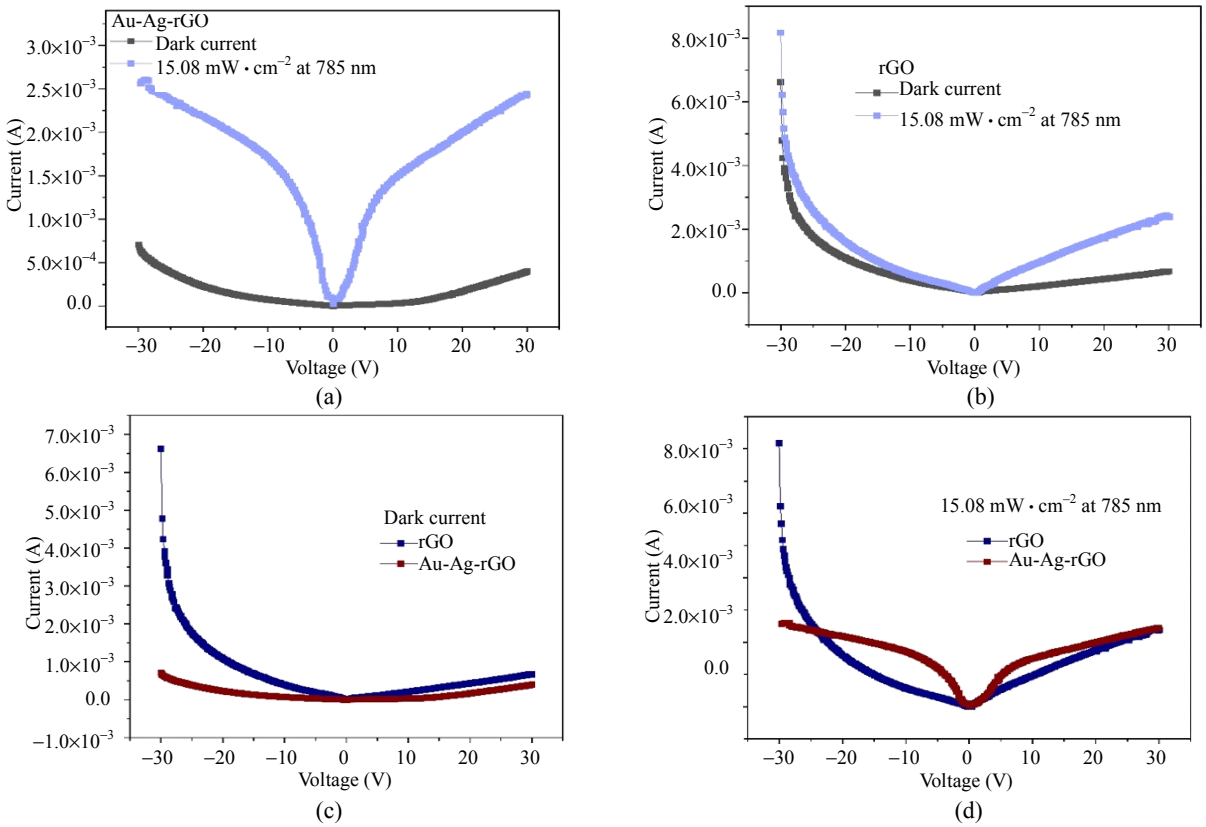

Fig. 4 Current-voltage (*I-V*) curves by device comparisons (a) – (b) as Au-Ag and rGO and by conditions (c) – (d) of the dark current and under the illumination of NIR LED 785 nm with 15.08 mW • cm^{-2} power intensity.

The study of photoexcitation of the device was continued by irradiating the devices with different power intensities, ranging from 31 μW • cm^{-2} to 15.08 mW • cm^{-2} as shown in Figs. 5(a) – 5(b). Essentially, the dark current was smaller than that under illumination of the NIR light source. Figures 5(a) – 5(b) exhibit that the current and light intensity are greatly dependent on each other, noticing the rise trend of the current when the light intensity increases. The excitation of the NIR light source incited the intraband and interband excitations of electrons which were known as hot carriers associated with the nonradiative plasmonic decay [39, 40].

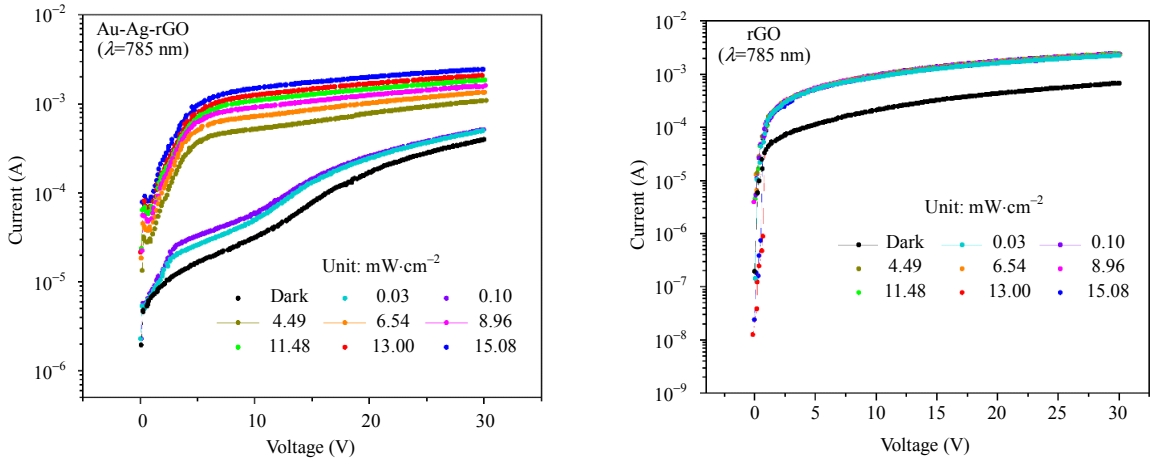

Fig. 5 *I-V* characteristics of (a) Au-Ag-rGO PD and (b) bare rGO PD illuminated by NIR LED 785 nm laser. 100% laser power intensity was 15.08 mW • cm^{-2}.

The potential for the NIR photodetector was further explored by calculating the responsivity (R), specific detectivity (D^*), and external quantum efficiency (EQE). These three figures of merit (FOM), R, D^*, and EQE, are crucial to assess the performance of the photodetector. The following part of this work moved on to describe in the further detail of the FOM of both photodetectors. The graphs plotted in Fig. 6 show all measurement values, which are in comparison between the bimetallic NPs and bare rGO at 785 nm illumination where Fig. 6(a) shows the comparison of photocurrent values. As indicated above, R is defined as the device sensitivity, which is described as the ratio of the photocurrent generated to illuminate the optical power intensity. It can be quantified as (2):

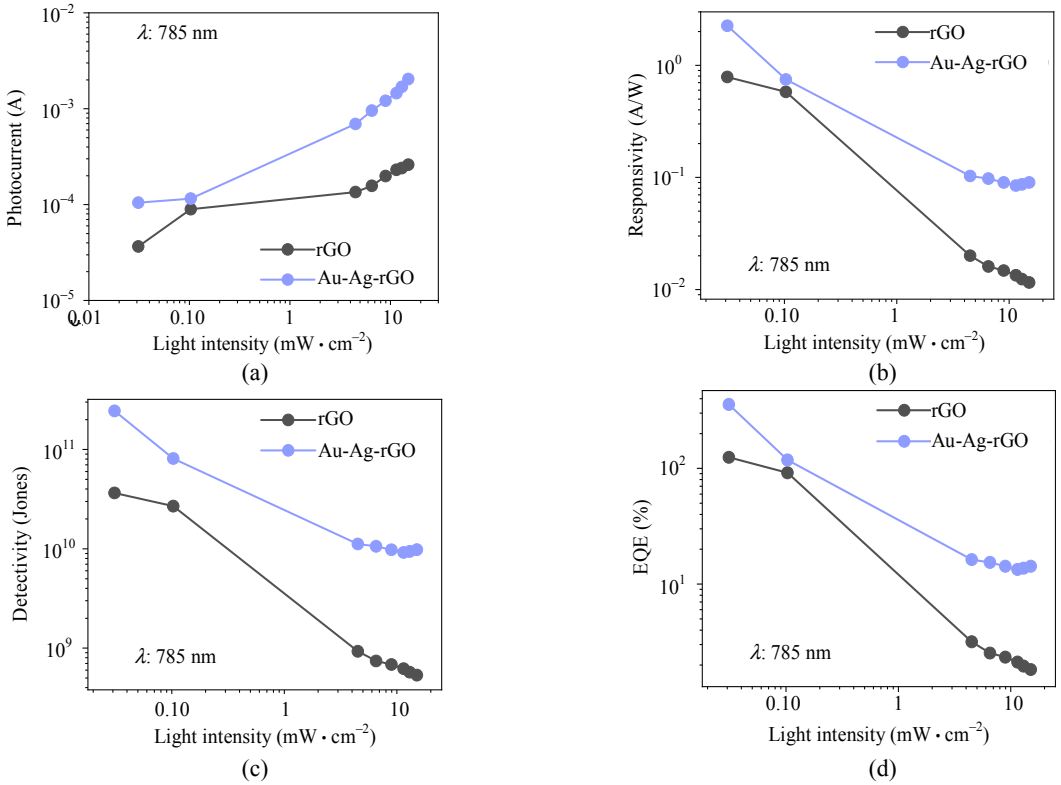

Fig. 6 Light intensity-dependent photocurrent (a), responsivity (b), detectivity (c), and EQE (d) of bimetallic NPs and bare rGO photodetectors under the illumination of 785 nm.

$$R = \frac{I_{ph}}{P_{opt} \cdot A} \tag{2}$$

where P_{opt} is the power density of incident light (in $mW \cdot cm^{-2}$), and A is the total effective illuminated area (in cm^2) of the device. Both devices of Au-Ag NPs and rGO PDs exhibit utmost R at the lowest power as illustrated in Fig. 6(b). Besides, with an increase in the light intensity, R shows a gradual decrease. The quantified data of R suggest that R is substantially escalating with the incorporation of the non-alloyed bimetallic Au-Ag nanoparticles. BMNPs-rGO PD displays a rise of R at $2.25\ A \cdot W^{-1}$ compared with the bare rGO with only $0.79\ A \cdot W^{-1}$. The increment shows almost up 3 times.

The next FOM parameter, detectivity (D^*) indicates the device capability to perceive a very small optical signal. It can be expressed as (3):

$$D^* = \frac{R \cdot \sqrt{A}}{\sqrt{2q \cdot I_d}} \tag{3}$$

where R is a responsivity, q is the electron charge, and I_d is the dark current of the device. Basically, the devices with the higher D^* are favorable to detect weak optical signals. From the calculation of D^*, it showed the same trend with the integration of non-alloyed BMNP in the PD as demonstrated in Fig. 6(c). The device displayed 2.45×10^{11} Jones, which was about 7 times greater than that of rGO PD.

EQE is to measure the ratio of the photocurrent to the number of incident photons by utilizing the responsivity value. This parameter can be calculated as (4):

$$\mathrm{EQE} = R \times \frac{1240}{\lambda} \times 100\% \quad (4)$$

where λ is the excitation wavelength of 785 nm. Both the EQEs of the bare rGO and BMNPs PD show the same pattern as well: high at the low power density and moderately decreasing with the rise of the light power intensity. Figure 6(d) illustrates the BMNPs-rGO PD showcase maximum of EQE of 356%, about three times greater than that of the bare rGO photodetector with the EQE of 124%. A summary of all FOM values are displayed in Table 1.

Table 1 Comparison of performance device between the rGO and bimetallic NPs.

Device	Responsivity ($A \cdot W^{-1}$)	Detectivity (Jones)	EQE ($\times 10^2$%)	Rise time (ns)	Fall time (ns)
BMNPs/rGO	2.25	2.45×10^{11}	3.56	32	186
rGO	0.79	3.65×10^{10}	1.24	502	17

The improvement in the EQE value happened due to that photons were absorbed by the metallic NPs, which enhanced the effect of carrier generation and recombination. These mechanisms could be simplified as a junction between the BMNPs and rGO/Si to facilitate the separation of excitons and the extraction of carriers, where the surface of the bimetallic of BMNPs possibly trapped minority carriers or depressed the carrier recombination in the rGO which improved hot carriers generated in the BMNPs. The hot carriers were able to be transferred into graphene which increased the photocurrent effects and also the near-field enhancement in the surface of the BMNPs which could be concluded as the plasmonic effect of light harvesting in graphene [41].

To further quantify, the time-dependent photocurrent (*I*-*t*) at the fixed bias of 10 V was reported. For both devices, various light power intensities of the NIR-LED 785 nm ranging from 2.09 $mW \cdot cm^{-2}$ to 15.08 $mW \cdot cm^{-2}$ were applied for the photoresponse measurement. The sharp rise and decay of the photocurrent were displayed in a continuous condition in on-off switching cycles of both devices. Each cycle of switching on and off maintained a likewise trend. The photocurrent of both devices also exhibited a significant rise along with an increase in the laser power intensities. Previous study has noted that this behavior was greatly due to the ultrafast hot electrons' injection and photothermally induced response [40].

From Figs. 7(a) – 7(b), it is observed that the BMNP device displays a higher current when the laser is switched on compared with the bare-rGO that exhibits a relatively lower photoresponse as the function of the laser light.

The enhancement of the localized electromagnetic field on the NPs also affected the photoresponse. This resulted from the collective oscillation of electrons and the photoexcited hot electrons from the BMNPs transfer to the conduction band of the rGO spontaneously. Figures 7(c) – 7(d) depicts the rise time (τ_r) and fall time (τ_f), which were evaluated from the measured photoresponse. These two parameters signified the time required while increasing to the 90% of the maximum photocurrent and decreasing to the 10% of the dark current, respectively. The BMNP device exhibited a shorter rise time, 32 ns, compared with the bare rGO, 502 ns. However, the fall time of the bare rGO revealed to be faster (17 ns) than that of the Au-Ag device (186 ns). The uniform and continuous five NIR switching on and off cycles displayed the sharp rise and fall of the photocurrent. This indicated that the operation of the non-alloyed BMNP-NIR photodetector demonstrated a fast response, good stability, and repeatability.

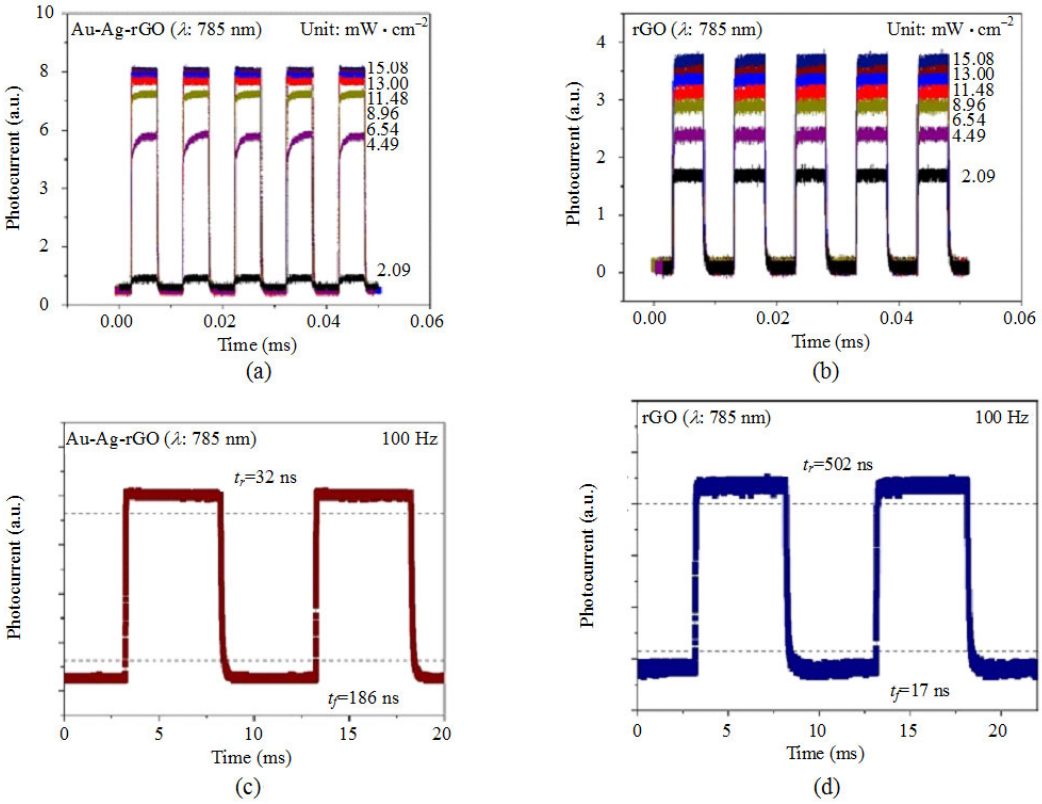

Fig. 7 *I-V* characteristics: (a) – (b) photoresponse for the BMNP-rGO and bare rGO devices from 2.09 mW · cm^{-2}–15.08 mW · cm^{-2}; (c) – (d) rising and falling edges for estimating the rise time (τ_r) and the fall time (τ_f) of the devices. All measurements were under the 785 nm laser illumination.

The use of the Cu-Ni bimetallic decorated graphene reported by A. Kumar *et al.* [42] showed the time constant of τ_r = 0.84 s followed the decay time as τ_f = 2.22 s and further decayed slowly to 93.19 s. S. Kunwar *et al.* [43] also reported that the photodetector of homogeneously alloyed Au-Ag on GaN (0001) exhibited the intensify responsivity (112 A · W^{-1}), detectivity (2.4×10^{12} Jones), and EQE (3.6×10^{4}%) at a low bias of 0.1 V with the greater Ag percentage, where the values comparison with the previous work are tabulated in Table 2. Overall, this work showed a higher performance by integrating the BMNPs of Au-Ag at the NIR region which was different from the previous reported work. The Au-Ag alloy NPs photodetector has shown evidence of a rapid photoresponse with the relatively small rise and fall time of less than 160 ms and 630 ms correspondingly.

Table 2 Comparison of the performance device between the rGO and bimetallic NPs.

Interface	Wavelength (nm)	Responsivity (A · W^{-1})	Detectivity (Jones)	EQE (%)	τ_r/τ_f	Ref.
rGO-CuNi NPs/SiO_2	White light	5.3×10^{-4}	–	–	0.83 s/2.22 s	[42]
Ag/rGO/Ag/quartz	632	0.23	–	88	–	[44]
AuNPs-rGO/SiO_2/Si	White light	3.8×10^{-2}	2.12×10^{8}	–	393 ns/399 ns	[45]
Ag NPs/NiO/rGO	365	3.95×10^{12}	24.46	8.0×10^{8}	8.4×10^{8}	[46]
Au-Ag NPs/GaN	112	2.4×10^{12}	3.6×10^{4}	1.6×10^{8}	6.3×10^{8}	[43]
rGO/Au-Ag BMNPs/Si	785	2.25	2.45×10^{11}	356	32 ns/186 ns	This work
rGO/Si	785	0.79	3.65×10^{10}	124	502 ns/17 ns	This work

4. Conclusions

In essence, the photoresponse of near infrared region photodetectors was investigated with incorporation of bimetallic nanoparticles of Au and Ag decorated on a reduced graphene oxide. The nanoparticles were formed by the process of the thin metallic layer fabrication using the electron-beam evaporation machine and continued by the solid-state dewetting method. After the modification of bimetallic layers, the BMNPs photocurrent significantly increased under the 785 nm illumination in comparison with the bare rGO. We believe this improvement in the heterostructure photodetector is attributed to the depletion region formed at BMNPs/rGO interfaces, light scattering, and the effect of localized surface plasmon resonance caused by metallic NPs. These findings indicate that the nanoparticles presence can maneuver the interaction of strong-light matter in the graphene layer, consequently greatly advancing NPs-rGO based detectors.

Acknowledgment

R. ZAKARIA would like to acknowledge Research University (RU) grant from University Malaya (Grant No. ST048-2021).

Reference

[1] V. Garg, B. S. Sengar, V. Awasthi, Aaryashree, P. Sharma, C. Mukherjee, *et al.*, "Localized surface plasmon resonance on Au nanoparticles: tuning and exploitation for performance enhancement in ultrathin photovoltaics," *RSC Advances*, 2016, 6(31): 26216–26226.

[2] T. Kiba, K. Masui, Y. Inomata, A. Furumoto, M. Kawamura, Y. Abe, *et al.*, "Control of localized surface plasmon resonance of Ag nanoparticles by changing its size and morphology," *Vacuum*, 2021, 192: 110432.

[3] C. de Melo, M. Jullien, Y. Battie, A. En. Naciri, J. Ghanbaja, F. Montaigne, *et al.*, "Tunable localized surface plasmon resonance and broadband visible photoresponse of Cu nanoparticles/ZnO surfaces," *ACS Applied Materials & Interfaces*, 2018, 10(47): 40958–40965.

[4] T. D. Kang and J. G. Yoon, "Optical characterization of surface plasmon resonance of Pt nanoparticles in TiO_2-SiO_2 nanocomposite films," *Journal of Applied Physics*, 2017, 122(13): 134302.

[5] E. Hutter and J. H. Fendler, "Exploitation of localized surface plasmon resonance," *Advanced Materials*, 2004, 16(19): 1685–1706.

[6] K. Okamoto, I. Niki, A. Shvartser, Y. Narukawa, T. Mukai, and A. Scherer, "Surface-plasmon-enhanced light emitters based on InGaN quantum wells," *Nature Materials*, 2004, 3(9): 601–605.

[7] K. S. Hamdan, S. M. Abdullah, K. Sulaiman, and R. Zakaria, "Effects of silver nanoparticles towards the efficiency of organic solar cells," *Applied Physics A*, 2013, 115(1): 63–68.

[8] V. E. Ferry, M. A. Verschuuren, H. B. T. Li, E. Verhagen, R. J. Walters, R. E. I. Schropp, *et al.*, "Light trapping in ultrathin plasmonic solar cells," *Optics Express*, 2010, 18(S2): A237–A245.

[9] J. Zhang, X. Zhang, J. Li, Z. Ma, B. Leng, Q. Xia, *et al.*, "Simultaneous visible and ultraviolet photoresponse improvement of MoS_2/ZnO heterostructure photodetector via direct resonant coupling of Au nanoparticles localized surface plasmon resonance," *Optical Materials*, 2022, 124: 111997.

[10] N. Patra, M. Manikandan, V. Singh, and I. Palani, "Investigations on LSPR effect of Cu/Al nanostructures on ZnO nanorods towards photodetector applications," *Journal of Luminescence*, 2021, 238: 118331.

[11] S. Valkov, M. Ormanova, and P. Petrov, "Electron-beam surface treatment of metals and alloys: techniques and trends," *Metals*, 2020, 10(9): 1219.

[12] K. T. Lin, H. Lin, and B. Jia, "Plasmonic nanostructures in photodetection, energy conversion and beyond," *Nanophotonics*, 2020, 9(10): 3135–3163.

[13] J. Guo, Z. Wu, Y. Li, and Y. Zhao, "Design of plasmonic photodetector with high absorptance and nano-scale active regions," *Optics Express*, 2016, 24(16): 18229–18243.

[14] B. Ezhilmaran, A. Patra, S. Benny, M. R. Sreelakshmi, V. V. Akshay, S. Venkataprasad Bhat, *et al.*, "Recent developments in the photodetector applications of Schottky diodes based on 2D

materials," *Journal of Materials Chemistry C*, 2021, 9(19): 6122–6150.
[15] Z. Lou, Z. Liang, and G. Shen, "Photodetectors based on two dimensional materials," *Journal of Semiconductors*, 2016, 37(9): 091001.
[16] C. Liu, J. Guo, L. Yu, J. Li, M. Zhang, H. Li, *et al.*, "Silicon/2D-material photodetectors: from near-infrared to mid-infrared," *Light: Science & Applications*, 2021, 10(1): 123.
[17] Y. Yu, F. Miao, J. He, and Z. Ni, "Photodetecting and light-emitting devices based on two-dimensional materials," *Chinese Physics B*, 2017, 26(3): 036801.
[18] C. K. Liao, J. Phan, M. Herrera, and M. A. Mahmoud, "Modifying the band gap of semiconducting two-dimensional materials by polymer assembly into different structures," *Langmuir*, 2019, 35(14): 4956–4965.
[19] P. Szirmai, B. G. Márkus, J. C. Chacón-Torres, P. Eckerlein, K. Edelthalhammer, J. M. Englert, *et al.*, "Characterizing the maximum number of layers in chemically exfoliated graphene," *Scientific Reports*, 2019, 9(1): 19480.
[20] D. Chen, Y. Xin, B. Lu, X. Pan, and Z. Ye, "Self-powered ultraviolet photovoltaic photodetector based on graphene/ZnO heterostructure," *Applied Surface Science*, 2020, 529: 147087.
[21] N. A. Zulkifli, K. Park, J. W. Min, B. S. Ooi, and C. L. Tan, "A highly sensitive, large area, and self-powered UV photodetector based on coalesced gallium nitride nanorods/graphene/silicon (111) heterostructure," *Applied Physics Letters*, 2020, 117(19): 191103.
[22] B. Lesiak, G. Trykowski, J. Toth, S. Biniak, L. Kover, N. Rangam, *et al.*, "Chemical and structural properties of reduced graphene oxide-dependence on the reducing agent," *Journal of Materials Science*, 2021, 56(5): 3738–3754.
[23] J. Liu, Y. Yin, L. Yu, Y. Shi, D. Liang, and D. Dai, "Silicon-graphene conductive photodetector with ultra-high responsivity," *Scientific Reports*, 2017, 7(1): 40904.
[24] Q. Wang, J. Lai, and D. Sun, "Review of photo response in semiconductor transition metal dichalcogenides based photosensitive devices," *Optical Materials Express*, 2016, 6(7): 2313–2327.
[25] Y. Ding, Z. Cheng, X. Zhu, K. Yvind, J. Dong, M. Galili, *et al.*, "Ultra-compact integrated graphene plasmonic photodetector with bandwidth above 110GHz," *Nanophotonics*, 2020, 9(2): 317–325.
[26] Q. Hu, Y. Cao, Y. Liu, Y. Wang, C. Wang, J. L. Zhu, *et al.*, "Ultra-wideband self-powered photodetector based on suspended reduced graphene oxide with asymmetric metal contacts," *RSC Advances*, 2021, 11(32): 19482–19491.
[27] Y. Su, Z. Guo, W. Huang, Z. Liu, T. Gong, Y. He, *et al.*, "Ultra-sensitive graphene photodetector with plasmonic structure," *Applied Physics Letters*, 2016, 109(17): 173107.
[28] L. Cheng, G. Zhu, G. Liu, and L. Zhu, "FDTD simulation of the optical properties for gold nanoparticles," *Materials Research Express*, 2020, 7(12): 125009.
[29] L. Han, T. Guo, C. Xie, P. Xu, J. Lao, X. Zhang, *et al.*, "Specific detection of aquaporin-2 using plasmonic tilted fiber grating sensors," *Journal of Lightwave Technology*, 2017, 35(16): 3360–3365.
[30] C. L. Tan, S. J. Jang, and Y. T. Lee, "Localized surface plasmon resonance with broadband ultralow reflectivity from metal nanoparticles on glass and silicon subwavelength structures," *Optics Express*, 2012, 20(16): 17448–17455.
[31] C. L. Tan, S. J. Jang, Y. M. Song, K. Alameh, and Y. T. Lee, "Bimetallic non-alloyed NPs for improving the broadband optical absorption of thin amorphous silicon substrates," *Nanoscale Research Letters*, 2014, 9(1): 1–6.
[32] K. G. Zhou, N. N. Mao, H. X. Wang, Y. Peng, and H. L. Zhang, "A mixed-solvent strategy for efficient exfoliation of inorganic graphene analogues," *Angewandte Chemie*, 2011, 123(46): 11031–11034.
[33] S. Schöche, N. Hong, M. Khorasaninejad, A. Ambrosio, E. Orabona, P. Maddalena, *et al.*, "Optical properties of graphene oxide and reduced graphene oxide determined by spectroscopic ellipsometry," *Applied Surface Science*, 2017, 421: 778–782.
[34] K. C. Lee, S. J. Lin, C. H. Lin, C. S. Tsai, and Y. J. Lu, "Size effect of Ag nanoparticles on surface plasmon resonance," *Surface and Coatings Technology*, 2008, 202(22): 5339–5342.
[35] M. Kang, M. S. Ahn, Y. Lee, and K. H. Jeong, "Bioplasmonic alloyed nanoislands using dewetting of bilayer thin films," *ACS Applied Materials & Interfaces*, 2017, 9(42): 37154–37159.
[36] N. S. Rohizat, A. H. A. Ripain, C. S. Lim, C. L. Tan, and R. Zakaria, "Plasmon-enhanced reduced graphene oxide photodetector with monometallic of Au and Ag nanoparticles at VIS-NIR region," *Scientific Reports*, 2021, 11(1): 1–10.
[37] Z. Fang, Z. Liu, Y. Wang, P. M. Ajayan, P. Nordlander, and N. J. Halas, "Graphene-Antenna Sandwich Photodetector," *Nano Letters*, 2012, 12(7): 3808–3813.
[38] S. Abbaszadeh, N. Allec, and K. Karim, "Characterization of low dark-current lateral amorphous-selenium metal-semiconductor-metal photodetectors," *IEEE Sensors Journal*, 2013, 13(5): 1452–1458.
[39] M. Valenti, A. Venugopal, D. Tordera, M. P. Jonsson, G. Biskos, A. Schmidt-Ott, *et al.*, "Hot carrier generation and extraction of plasmonic alloy nanoparticles," *ACS Photonics*, 2017, 4(5): 1146–1152.
[40] L. Wen, Y. Chen, W. Liu, Q. Su, J. Grant, Z. Qi,

et al., "Enhanced photoelectric and photothermal responses on silicon platform by plasmonic absorber and Omni-Schottky junction," *Laser & Photonics Reviews*, 2017, 11(5): 1700059.

[41] D. H. Shin and S. H. Choi, "Graphene-based semiconductor heterostructures for photodetectors," *Micromachines*, 2018, 9(7): 350.

[42] A. Kumar, S. Husale, A. Srivastava, P. Dutta, and A. Dhar, "Cu-Ni nanoparticle-decorated graphene based photodetector," *Nanoscale*, 2014, 6(14): 8192–8198.

[43] S. Kunwar, S. Pandit, J. H. Jeong, and J. Lee, "Improved photoresponse of UV photodetectors by the incorporation of plasmonic Nanoparticles on GaN through the resonant coupling of localized surface plasmon resonance," *Nano-Micro Letters*, 2020, 12(1): 91.

[44] M. A. Khan, K. L. Kumawat, K. K. Nanda, and S. B. Krupanidhi, "Reduced graphene oxide-based broad band photodetector and temperature sensor: effect of gas adsorption on optoelectrical properties," *Journal of Nanoparticle Research*, 2018, 20(11): 1–11.

[45] N. S. Abd Aziz, Y. Nakajima, H. Sato, T. Maekawa, and A. M. Hashim, "One-pot green synthesis of Ag nanoparticle-decorated reduced graphene oxide composites: effect of Ag/graphene oxide volume ratio and its demonstration as low-voltage on-chip photodetector," *Journal of Materials Science*, 2018, 53(16): 11620–11632.

[46] P. Joshna, S. R. Gollu, P. M. P. Raj, B. V. V. S. N. P. Rao, P. Sahatiya, and S. Kundu, "Plasmonic Ag nanoparticles arbitrated enhanced photodetection in p-NiO/n-rGO heterojunction for future self-powered UV photodetectors," *Nanotechnology*, 2019, 30(36): 365201.